

Composition-selective fabrication of ordered intermetallic Au–Cu nanowires and their application to nano-size electrochemical glucose detection

Si-In Kim^{1,4}, Gayoung Eom^{1,2,4}, Mijeong Kang¹, Taejoon Kang²,
Hyoban Lee¹, Ahreum Hwang^{1,2}, Haesik Yang³ and Bongsoo Kim¹

¹ Department of Chemistry, KAIST, Daejeon 305-701, Korea

² BioNanotechnology Research Center and BioNano Health Guard Research Center, KRIBB, Daejeon 305-806, Korea

³ Department of Chemistry, Pusan National University, Busan 609-735, Korea

E-mail: hyang@pusan.ac.kr and bongsoo@kaist.ac.kr

Received 29 December 2014, revised 24 April 2015

Accepted for publication 24 April 2015

Published 27 May 2015



CrossMark

Abstract

Bimetallic nanostructures can provide distinct and improved physicochemical properties by the coupling effect of the two metal components, making them promising materials for a variety of applications. Herein, we report composition-selective fabrication of ordered intermetallic Au–Cu nanowires (NWs) by two-step chemical vapor transport method and their application to nano-electrocatalytic glucose detection. Ordered intermetallic Au₃Cu and AuCu₃ NWs are topotaxially fabricated by supplying Cu-containing chemicals to pre-synthesized single-crystalline Au NW arrays. The composition of fabricated Au–Cu NWs can be selected by changing the concentration of Cu-containing species. Interestingly, Au₃Cu NW electrodes show unique electrocatalytic activity for glucose oxidation, allowing us to detect glucose without interference from ascorbic acid. Such interference-free detection of glucose is attributed to the synergistic effect, induced by incorporation of Cu in Au. We anticipate that Au₃Cu NWs could show possibility as efficient nano-size electrochemical glucose sensors and the present fabrication method can be employed to fabricate valuable ordered intermetallic nanostructures.

 Online supplementary data available from stacks.iop.org/NANO/26/245702/mmedia

Keywords: nanowire, intermetallic, nanoelectrode

(Some figures may appear in colour only in the online journal)

1. Introduction

In the past years, nanostructures have been emerging as a new class of materials due to their unique and interesting characteristics [1–4]. Bimetallic nanostructures can often provide distinct and more improved physical and chemical properties than monometallic nanostructures due to the coupling effect of the two metal components [5–8]. Specifically, structurally

ordered intermetallic nanostructures with a definite stoichiometric composition and an ordered lattice structure can show dramatically improved magnetic, catalytic, and thermal properties, making them promising materials for a variety of applications [9–14]. For example, ordered intermetallic Au–Cu, Pt–Ti, and Pt–Cu nanomaterials exhibit high catalytic activity for diverse reactions [12, 15–19]. Moreover, chemically ordered FePt nanoparticles showed enhancements in Curie temperature, coercivity, and thermal stability [14]. Ordered intermetallic nanostructures have been extensively

⁴ These authors contributed equally to this work.

developed and reported on [20–24]. Since most of the structures have been synthesized in the solution phase by employing surfactants, residual surfactants often block the surface of nanostructures, making it difficult to fully utilize the physical and chemical properties of the nanostructures [12, 16, 18]. Recently, Zhuang *et al* and Abruña *et al* reported a one-pot reduction method and an impregnation reduction method for the synthesis of ordered intermetallic AuCu and Pt₃Co nanoparticles without surfactants, respectively [11, 25]. These nanoparticles showed superior catalytic performance for the oxygen reduction reaction, indicating superb properties of surfactant-free ordered intermetallic nanostructures.

Herein, we report vapor-phase synthesis of structurally ordered intermetallic Au–Cu nanowires (NWs) and their electrocatalytic performance for glucose oxidation. Single-crystalline Au₃Cu and AuCu₃ NWs were topotaxially synthesized by supplying Cu-containing species onto the pre-synthesized Au NWs, and the compositions of the Au–Cu NWs were selectively determined by adjusting the concentration of the Cu-containing species. Furthermore, as-synthesized Au₃Cu NW electrodes show a newly generated glucose oxidation current wave, allowing us to detect glucose selectively even in the presence of ascorbic acid (AA).

The present study highlights the following. First, single-crystalline Au–Cu NWs that have structurally ordered intermetallic nanostructures are, to the best of our knowledge, synthesized for the first time. Quite importantly, their surfaces are clean and surfactant-free. Second, Au₃Cu NW electrodes show selective electrocatalytic activity for glucose oxidation and thus they suggest possible application as an interference-free electrochemical glucose nano-detector that may probe glucose concentration in a single cell in real time without cell damage [26]. Detection of glucose without interference from AA could help us to develop enzyme-free glucose detection [27–33]. Third, the present simple synthesis method that employs a topotaxial transformation can broaden the range of ordered intermetallic nanostructures. We anticipate that diverse types of ordered intermetallic nanostructures may become valuable materials in a variety of research fields.

2. Experimental section

2.1. Materials

Au lump and CuI powder (99.999%) were purchased from Sigma-Aldrich. D-(+)-glucose, L-AA, potassium chloride and potassium ferricyanide(III) were purchased from Sigma. Sulfuric acid was purchased from Sigma-Aldrich. Sodium hydroxide was purchased from Junsei Chemical Co., Ltd. A W tip was purchased from GGB Industries Inc. Conducting adhesive solution was purchased from Norland Products, Inc.

2.2. Synthesis of Au–Cu NWs

Ordered intermetallic Au–Cu NWs were synthesized in a 1 in diameter quartz tube by using a horizontal hot-wall furnace system. First, single-crystalline Au NWs were synthesized by

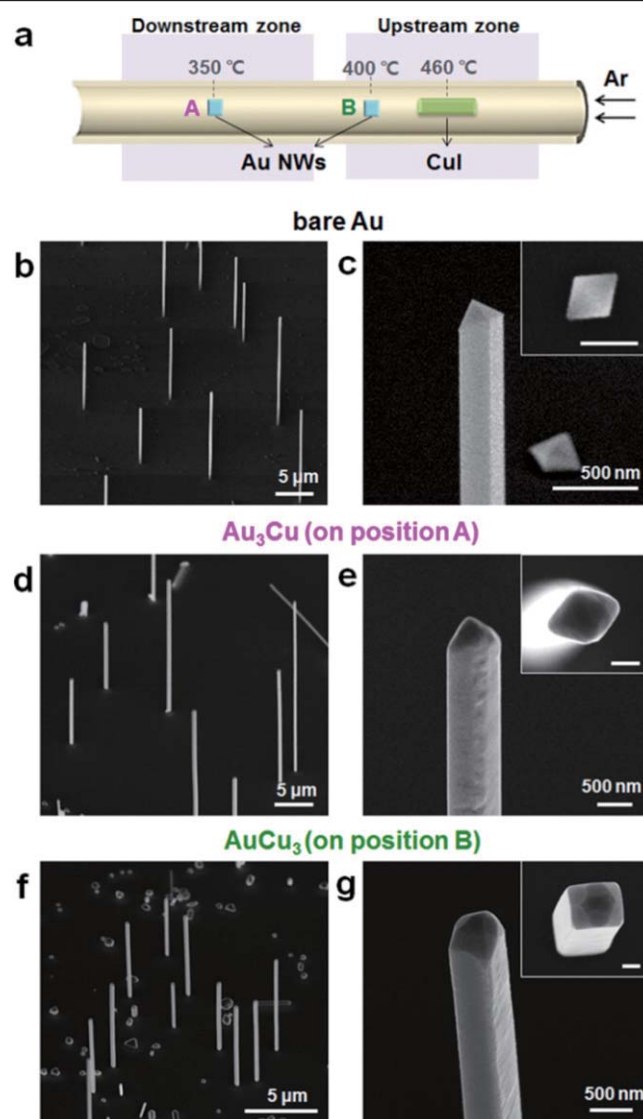


Figure 1. (a) Schematic illustration of the experimental setup for the synthesis of ordered intermetallic Au–Cu NWs. The setup consists of a horizontal quartz tube furnace system with two independently controllable heating zones. Au₃Cu and AuCu₃ NWs are synthesized by the reaction between the CuI precursor and Au NW-grown substrate placed at positions A and B, respectively. 45° tilted-view SEM images of vertically grown (b), (c) Au, (d), (e) Au₃Cu, and (f), (g) AuCu₃ NWs on *c*-cut sapphire substrates. Insets of (c), (e) and (g) are top-view SEM images of each NW. Inset scale bars denote 200 nm.

previously reported method [34]. Briefly, a Au lump in an alumina boat was placed at the center of heating zone and 5 × 5 mm² sapphire substrates were placed 5–7 cm away from the boat to the downstream side. The alumina boat was heated at 1100–1150 °C for 90 min with 100 sccm Ar flow rate, maintaining the chamber pressure at 8–15 Torr. Next, CuI powder in an alumina boat was placed at the center of upstream zone and as-synthesized Au NWs on sapphire substrates were placed ~18 cm away from the boat to the downstream side (position A of figure 1(a)). The boat was heated at 460 °C for 20 min with 100 sccm Ar flow rate, maintaining the chamber pressure at 10 Torr. Finally,

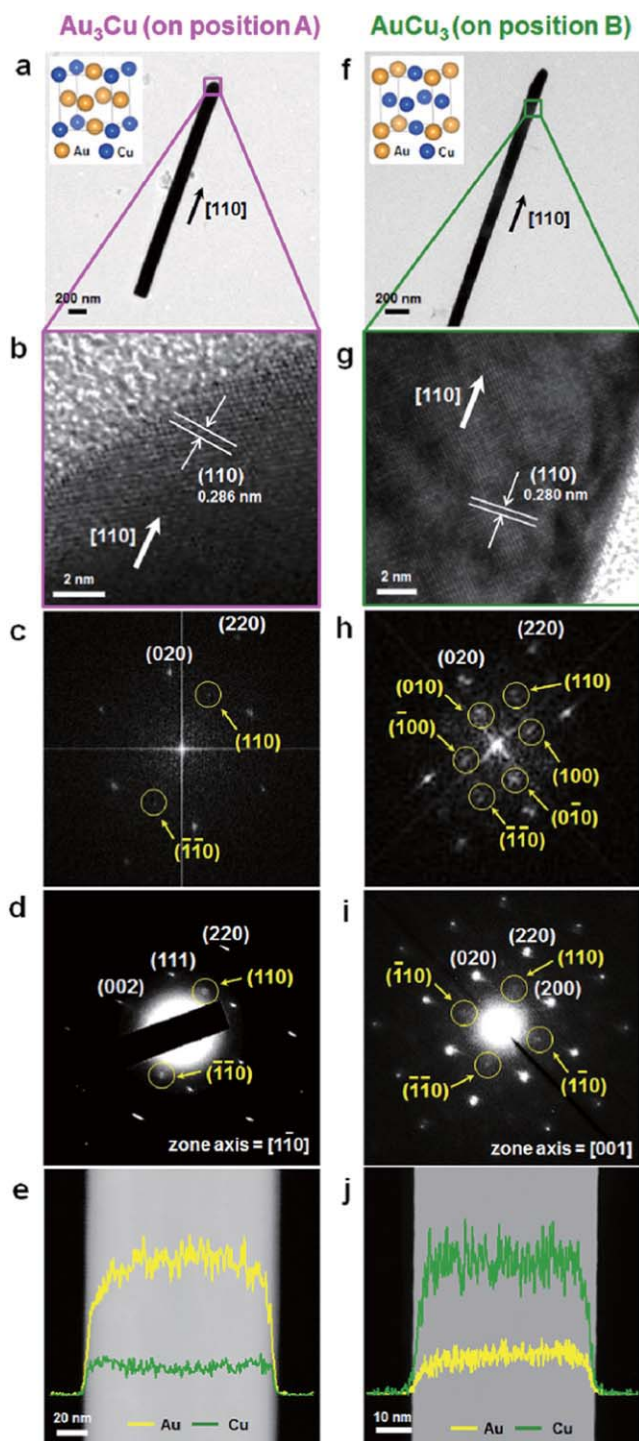


Figure 2. (a) Low-resolution TEM images, (b) HRTEM images of the pink square in (a), (c) FFT patterns of (b), (d) SAED patterns, (e) EDS line profiles of ordered intermetallic of Au_3Cu ; (f)–(j) those of AuCu_3 NWs. Both NWs have an fcc crystal structure with a $[110]$ growth direction. HRTEM images are obtained from the green square in (f). Diffraction spots such as $\{100\}$ and $\{110\}$ peaks marked by yellow circles in (c), (d), (h) and (i) clearly indicate the formation of ordered intermetallic structures, not alloy structures, for both Au_3Cu and AuCu_3 . Au (yellow lines) and Cu (green lines) atoms are uniformly distributed in both NWs with a stoichiometry of Au:Cu $\sim 73:27$ and $23:77$ in (e) and (j), respectively, further demonstrating formation of ordered intermetallic Au_3Cu and AuCu_3 NWs, respectively. Insets of (a), (f) are the schematics of crystal structure for Au_3Cu and AuCu_3 , respectively.

topotaxially grown Au_3Cu NWs were obtained. For the synthesis of AuCu_3 NWs, the same experimental procedure was carried out except the position of pre-synthesized Au NWs, ~ 5 cm away from CuI powder (position B of figure 1(a)).

2.3. Fabrication of NW electrodes

Au, Au_3Cu , and AuCu_3 NW electrodes were fabricated by using a micromanipulator under optical monitoring (figure S5 in the supporting information) [26]. A W tip equipped to a micromanipulator closely approached to a NW grown on a sapphire substrate. By softly touching the NW, the W tip picked up the NW from the substrate by using van der Waals attraction. To enhance the conductivity and robustness of NW electrodes, the junction area of W tip and NW was coated with a UV curing conducting adhesive solution and then exposed to UV light for 2 h.

2.4. Instrumentation

Scanning electron microscope (SEM) images were taken on a Phillips XL30S and Nova 230. Transmission electron microscopy (TEM) and high-resolution TEM (HRTEM) images, selected-area electron diffraction (SAED) patterns, and energy-dispersive x-ray spectroscopy (EDS) spectra were taken on a JEOL JEM-2100F operated at 200 kV. For the TEM analysis, as-synthesized NWs were dispersed in ethanol, and then a drop of the solution was drop-evaporated onto a carbon film-coated molybdenum TEM grid. The x-ray diffraction (XRD) patterns of the specimen were recorded on a Rigaku D/max-rc (12 kW) diffractometer operated at 30 kV and 60 mA with filtered $\text{CuK}\alpha$ radiation. Electrochemical measurements were carried out by using a CHI 660D electrochemical workstation (CH instruments, USA) in a three-electrode cell. The working electrodes were as-prepared NW electrodes and a Pt wire was used as the counter electrode. An Ag/AgCl (3 M NaCl) electrode was employed as the reference electrode and sodium hydroxide was used as electrolytes. The potential scan was taken from 0.3 to 0.7 V (versus Ag/AgCl) at a scan rate of 100 mV s^{-1} . All solutions were prepared in a 100 mM NaOH with triply distilled water and saturated with nitrogen gas for 10 min before electrochemical measurements. Assuming NWs as pseudo-cylindrical shape, the geometric area was calculated with diameter of NWs from SEM image. The measured current was normalized to the geometric area of the working electrode.

3. Results and discussion

3.1. Synthesis of structurally ordered intermetallic Au–Cu NWs

Ordered intermetallic Au–Cu NWs were synthesized through a two-step chemical vapor transport (CVT) method using a hot-wall quartz tube furnace system. First, single-crystalline Au NWs were epitaxially grown on a *c*-cut sapphire substrate [34]. Second, ordered intermetallic Au–Cu NWs were topotaxially fabricated by supplying Cu-containing chemicals to

as-synthesized Au NWs (figure 1(a)). The composition of Au–Cu NWs can be controlled by adjusting the position of Au NW-grown substrate in a quartz tube. Au₃Cu NWs were obtained by placing Au NW-grown substrate ~18 cm from the CuI precursor (position A of figure 1(a)). AuCu₃ NWs were synthesized by placing Au NW-grown substrate ~5 cm from the CuI precursor (position B of figure 1(a)). All other reaction conditions, including CuI heating temperature, pressure, and carrier gas flow rate, were kept the same. Figures 1(b)–(g) displays SEM images of synthesized NWs. Figures 1(b) and (c) show vertically grown Au NWs on a *c*-cut sapphire substrate. Single-crystalline Au NWs have a half-octahedral tip and rhombic cross-section (inset of figure 1(c)) with clear facets and extremely smooth surfaces. Figures 1(d) and (e) illustrate Au₃Cu NWs synthesized at position A. Ordered intermetallic Au₃Cu NWs retain a rhombic cross-section (inset of figure 1(e)) but have rough surfaces. Figures 1(f) and (g) show AuCu₃ NWs synthesized at position B. Unlike Au and Au₃Cu NWs, the cross-section of AuCu₃ NWs is rectangular (inset of figure 1(g)).

The compositions and structures of Au–Cu NWs were characterized by TEM analyses. Figures 2(a) and (f) show low-resolution TEM images of Au₃Cu and AuCu₃ NWs, respectively. HRTEM images of figures 2(b) and (g) are obtained from the pink square in figure 2(a) and the green square in figure 2(f), respectively. HRTEM images, fast Fourier transform (FFT), and SAED patterns in figures 2(b)–(d) verify that Au₃Cu NWs have a face-centered cubic (fcc) crystal structure with a [110] growth direction, the same as Au NWs. AuCu₃ NWs also have an fcc crystal structure and a [110] growth direction (figures 2(g)–(i)). The schematics of crystal structure for Au₃Cu and AuCu₃ are exhibited in insets of figures 2(a) and (f), respectively. Both Au₃Cu and AuCu₃ NWs clearly show lattice fringes in HRTEM images and spot diffractions in SAED patterns, demonstrating single-crystallinity. Most importantly, the {110} peaks in the FFT and SAED patterns of figures 2(c) and (d) (marked by yellow circles) clearly indicate the formation of ordered intermetallic Au₃Cu structures. Likewise, the {100} and {110} peaks in figures 2(h) and (i) (indicated by yellow circles) obviously show the formation of ordered intermetallic structures for AuCu₃ NWs [24]. Elemental line profile analyses by EDS found that Au and Cu atoms are uniformly distributed in both NWs with a stoichiometry of Au:Cu = ~73:27 and 23:77, respectively (figures 2(e) and (j)), further confirming successful formation of ordered intermetallic Au₃Cu and AuCu₃ NWs, respectively. This growth method could be extended to nanoplates. When Cu-containing chemicals are supplied to the single-crystalline Au nanoplates, grown on an *m*-cut sapphire substrate using this CVT method, ordered intermetallic Au₃Cu and AuCu₃ nanoplates are synthesized (figures S1 and S2 in the supporting information).

Figure 3 displays the XRD spectra of Au, Au₃Cu and AuCu₃ NWs, indicating that all peaks correspond to the reflections of fcc Au (JCPDS #65-8601), Au₃Cu (JCPDS #00-034-1302), and AuCu₃ phase (JCPDS #35-1357). The peaks of (111), (200), and (220) in Au, Au₃Cu and AuCu₃ NWs are gradually shifted to higher 2 theta values with increasing Cu

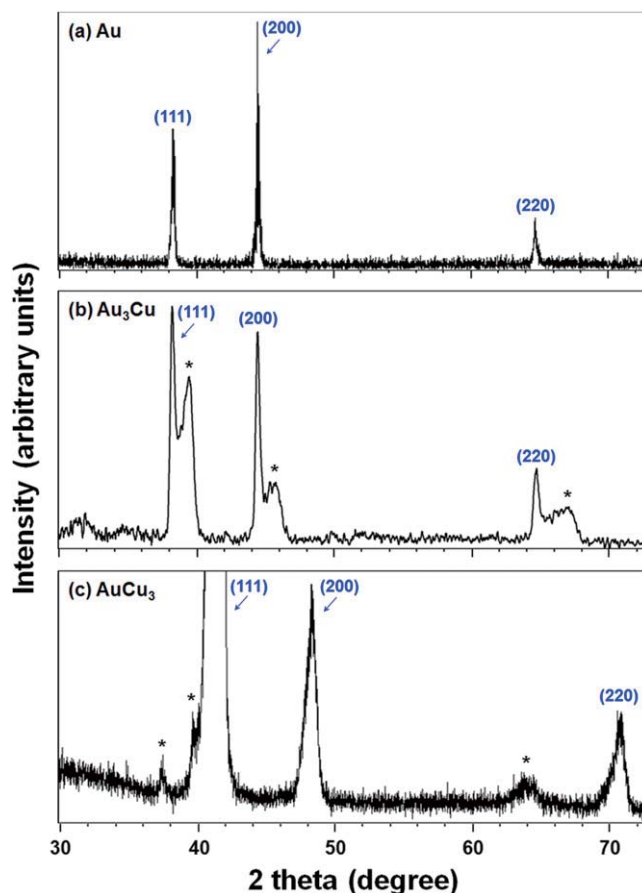
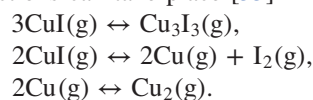


Figure 3. XRD spectra of (a) Au, (b) Au₃Cu, and (c) AuCu₃ NWs. The XRD patterns indicate that all peaks correspond to the reflections of Au (JCPDS #65-8601), Au₃Cu (JCPDS #00-034-1302), and AuCu₃ phase (JCPDS #35-1357), respectively. The peaks from sapphire substrate are marked by asterisk.

atomic ratio of NWs. The XRD spectra of Au₃Cu and AuCu₃ NWs are also in good agreement with previously reported Au₃Cu nanocubes and AuCu₃ particles [18, 24].

When we use CuI as a precursor in the synthesis of ordered intermetallic Au–Cu NWs, the following gas-phase reactions can take place [35]



Most of the Cu-containing species appearing in this reaction, including CuI, Cu₃I₃, Cu, and Cu₂, can supply Cu atoms either by direct collision or collision induced dissociation to Au NWs. The resultant Cu atoms can diffuse into Au NWs and form Au–Cu NWs [36]. Synthesis of Au₃Cu or AuCu₃ NWs can be selected by adjusting the position of Au NW-grown substrate in a quartz tube furnace system. This selectivity is attributed to the concentration variance of the Cu-containing species along the quartz tube as our previous result of location-dependent selective synthesis [37]. The concentration of Cu-containing species generally decreases gradually from the upstream zone to the downstream zone, leading to the formation of Au₃Cu and AuCu₃ NWs in positions A and B, respectively.

The cross-sectional shape of ordered intermetallic AuCu₃ NWs differs from those of Au and Au₃Cu NWs (figure 1). When we carried out annealing in the absence of CuI precursor (figure S3 in the supporting information), Au NWs retained original rhombic cross-section and well-defined facet at both positions. Thus the cross-section change in AuCu₃ NW is not due to the annealing effect, but seems to be rather due to compositional change. When Au NWs are transformed into ordered intermetallic AuCu₃ NWs, Au atoms at the center of the faces in an fcc unit cell of Au are substituted with Cu atoms [24]. The lattice constant of AuCu₃ is 3.76 Å, which is closer to that of Cu (3.61 Å) than that of Au (4.08 Å). Note that the atomic radius of Au (1.74 Å) is significantly larger than that of Cu (1.45 Å). Ordered intermetallic Au₃Cu crystal with Au and Cu atoms at the center of the surface and each corner, respectively, has a lattice constant of 4.04 Å, which is quite close to that of Au [18]. In our previous result for the topotaxial synthesis of Au–Ag NWs [38], they form the alloy over a full range of composition (from 0 to 100%), not forming an intermetallic compound, which can be ascribed to very similar atomic radii of Au and Ag. It seems that such similar atomic radii also kept the same cross-section of the Au–Ag alloy NW [38]. In contrast, Au–Cu NWs exhibit several alloy–intermetallic transformations over the composition range according to phase diagram for Au–Cu system, which can be attributed to the significant size difference. Such a distinct lattice constant change by incorporation of a significant number of Cu atoms into Au NWs may have induced the cross-sectional shape modification of AuCu₃ NWs. The rough surfaces of Au₃Cu and AuCu₃ NWs are most likely caused by the etching effect of I₂ produced from the CuI precursor [35, 39].

To explore the formation mechanism of ordered intermetallic Au–Cu NWs, we investigated the EDS line profiles of Au–Cu NWs as we varied reaction time. Figures 4(a)–(e) display the EDS line profile results of Au–Cu NWs at reaction times of 0, 1, 3, 5, and 10 min, respectively. The NWs were synthesized at position B. A reaction time of 0 min means that the reaction was stopped immediately after the temperature of the upstream zone reached 460 °C. Figure 4(f) displays a plot of the Cu atomic composition in Au–Cu NWs versus the reaction time based on figures 4(a)–(e). The data represent the mean plus standard deviation from three measurements, overlapped with an exponentially fitted curve (blue curve in figure 4(f)). The Cu composition of the Au–Cu NWs was 40% at 0 min and gradually increased to 52, 68, 70, and 77% at 1, 3, 5, and 10 min, respectively. This graph illustrates that the Cu composition increases rapidly at an initial stage of the reaction, slows down after 3 min, and is saturated after 10 min.

It should be noted that the radial distribution of Cu atoms in the NW changes with the reaction time. At 0 min, Cu atoms are uniformly distributed over the whole volume of a NW (figure 4(a)). At 1, 3, and 5 min, more Cu atoms are located near the NW surface (figures 4(b)–(d)). At 10 min, Cu atoms are well spread over the whole NW (figure 4(e)). This distribution can be explained by the difference between the supply rate of Cu atoms onto the original Au NW and the

diffusion rate of Cu atoms into the Au NW. In the beginning (0 min), the supply rate of Cu atoms increases slowly with time and could be comparable to the internal diffusion rate. At 1 and 3 min, the supply rate of Cu atoms would get faster than the internal diffusion rate. Hence, Cu atoms are located near the NW surface. After the reaction time of 10 min, a stable and homogeneous AuCu₃ NW is formed by atomic rearrangement through internal diffusion. Based upon this observation, we deduce that a high surface area of Au NWs, a sufficient supply of Cu atoms, and enough thermal energy for atomic reordering enable the fast transformation from Au NWs to ordered intermetallic Au–Cu NWs [36, 40].

Additionally, the crystal stability and oxidation tendency of ordered intermetallic AuCu₃ NWs were tested. After being stored under ambient conditions at room temperature for 20 days, TEM analyses (figure S4 in the supporting information) reveal that no detectable copper oxide layer was formed, and the crystal structure was well maintained, indicating that the ordered intermetallic AuCu₃ NWs are fairly resistant to oxidation for 20 days. Alloying Cu with other metals can prevent Cu₂O surface island growth, thus exhibiting stabilizing effect against oxidation compared pure Cu [41].

3.2. Electrocatalytic activity of Au–Cu NW electrode

In order to investigate the electrochemical properties of Au, Au₃Cu and AuCu₃ NWs, we fabricated NW electrodes and measured cyclic voltammetry [26]. Figure 5(a) shows SEM image of as-prepared NW electrode attached on W tip. Figure 5(b) presents cyclic voltammograms (CVs) of Au (green curve), Au₃Cu (pink curve) and AuCu₃ (blue curve) NW electrodes in a 50 mM H₂SO₄. In CVs of ordered intermetallic Au₃Cu and AuCu₃ NW electrodes, weak peaks appear between 0.1 and 0.3 V, corresponding to the oxidation of copper, and typical anodic and cathodic peaks for Au oxide formation and its reduction are observed. Figure 5(c) presents CVs of Au₃Cu NW electrode in 20 mM K₃Fe(CN)₆ with or without 0.1 M KCl as supporting electrolyte. In both solutions, ordered intermetallic Au₃Cu NW electrode shows sigmoidal-shaped curves, indicating steady-state voltammetric response at Au₃Cu NW electrode. Even in the absence of supporting electrolyte, well-defined voltammetric curve was observed with similar half-wave potential ($E_{1/2}$) value, indicating that there was almost no effect of the Ohmic resistance. Because of such unique properties of NW electrode, Au₃Cu NW electrode can be applied in resistive media as well as electrolyte solution.

We explored electrooxidation properties of glucose on the ordered intermetallic Au–Cu NW electrodes. For enzyme-free glucose detection, it is critically important to distinguish glucose from the interfering species such as AA, uric acid, dopamine, fructose, sucrose, etc in blood. Among them AA and uric acid cause main interference in glucose detection because both are easily oxidized. Particularly, while AA is less contained than uric acid about 5 times in blood, AA is considered as more serious interfering species due to higher oxidation reactivity. Moreover, although the AA level (~0.1 mM) in blood is much lower than glucose level

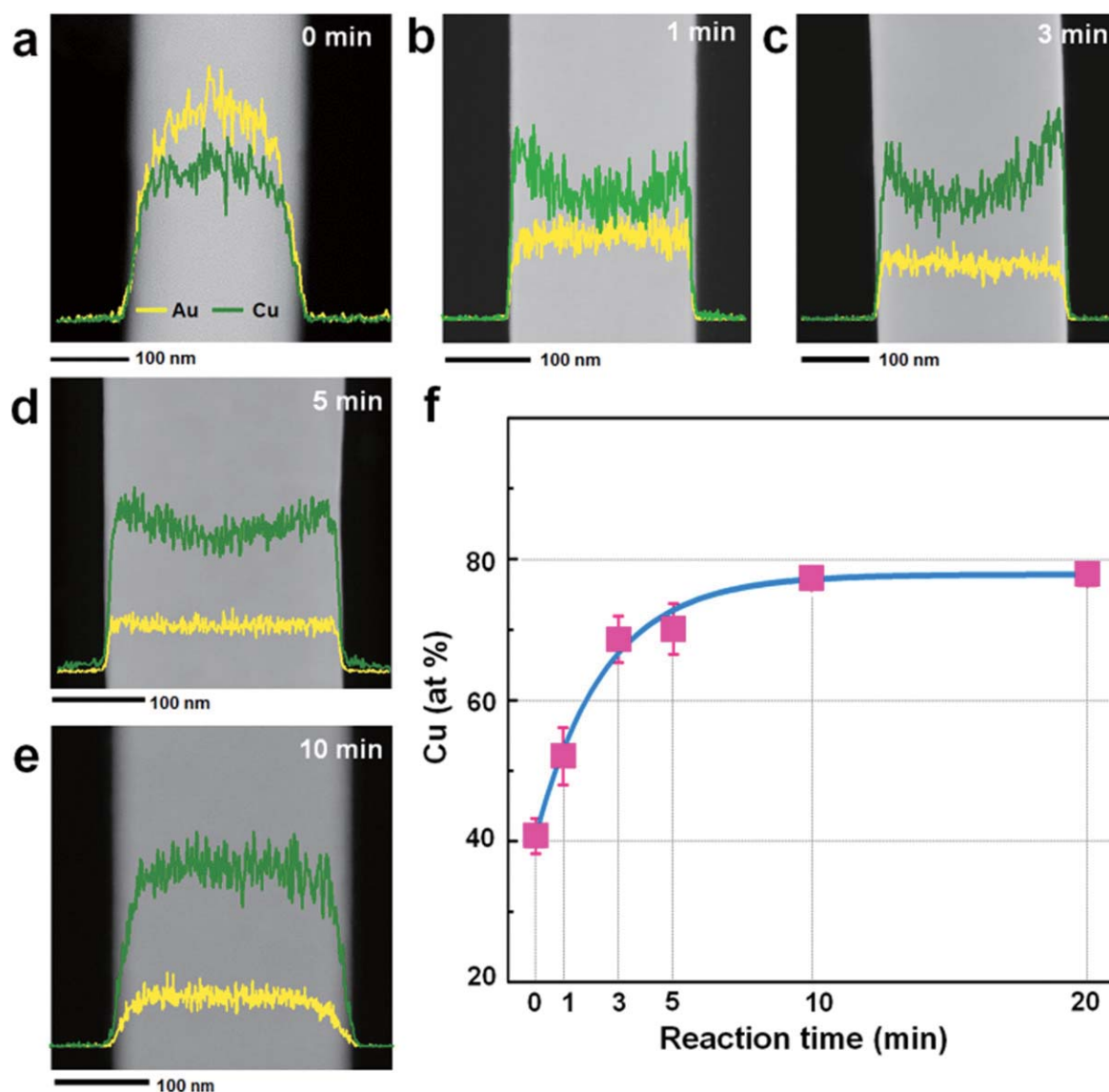


Figure 4. EDS line profiles of Au–Cu NWs prepared at reaction times of (a) 0, (b) 1, (c) 3, (d) 5, and (e) 10 min. (f) Plot of the Cu atomic ratio in Au–Cu NWs versus reaction time. The data represent the mean plus the standard deviation from three measurements, and the exponentially fitted curve is also presented (blue curve).

(3–8 mM), the oxidation current wave from AA is comparable to that from glucose at high potentials where the glucose oxidation starts, inducing detection error [42, 43]. Therefore, it is vital to selectively detect glucose in the potential range where AA is not oxidized. In many cases, the electrooxidation of organic molecules is clearly observed mainly in the reverse cathodic scan of CVs [44, 45]. This is because the poison often formed in the low potential is eliminated by oxidation in the high potential. In this experiment, the oxidation peak of glucose is barely observed in the anodic scan but clearly observed in the reverse cathodic scan after the electrode is oxidized up to 0.7 V at both the Au and Au₃Cu NW electrodes. The AuCu₃ NW is excluded from glucose detection because it became gradually thinner during the electrochemical measurements and its electrochemical properties changed.

Figure 6 shows reverse cathodic scans (–0.3–0.3 V) of CVs from Au and Au₃Cu NW electrodes in a 100 mM NaOH solution containing 4.0 mM glucose and/or 0.1 mM AA. In the reverse cathodic scans of a Au NW electrode, the anodic current peaks of glucose and AA appear at 0.03 and 0.02 V, respectively (red and green curves of figure 6(a)). Because the peak positions are overlapped, the electrochemical signals from glucose and AA are not distinguishable at a Au NW electrode. Figure 6(b) illustrates electrocatalytic activity of a Au₃Cu NW electrode for the oxidation of glucose and AA. Quite importantly, the oxidation current waves of glucose and AA show different behavior. While AA shows an oxidation peak at 0.02 V (green curve), glucose has additional distinct wave at –0.16 V marked by a pink arrow in figure 6(b) in addition to the strong peak at 0.03 V (red curve). Since the additional current wave for the glucose oxidation is observed

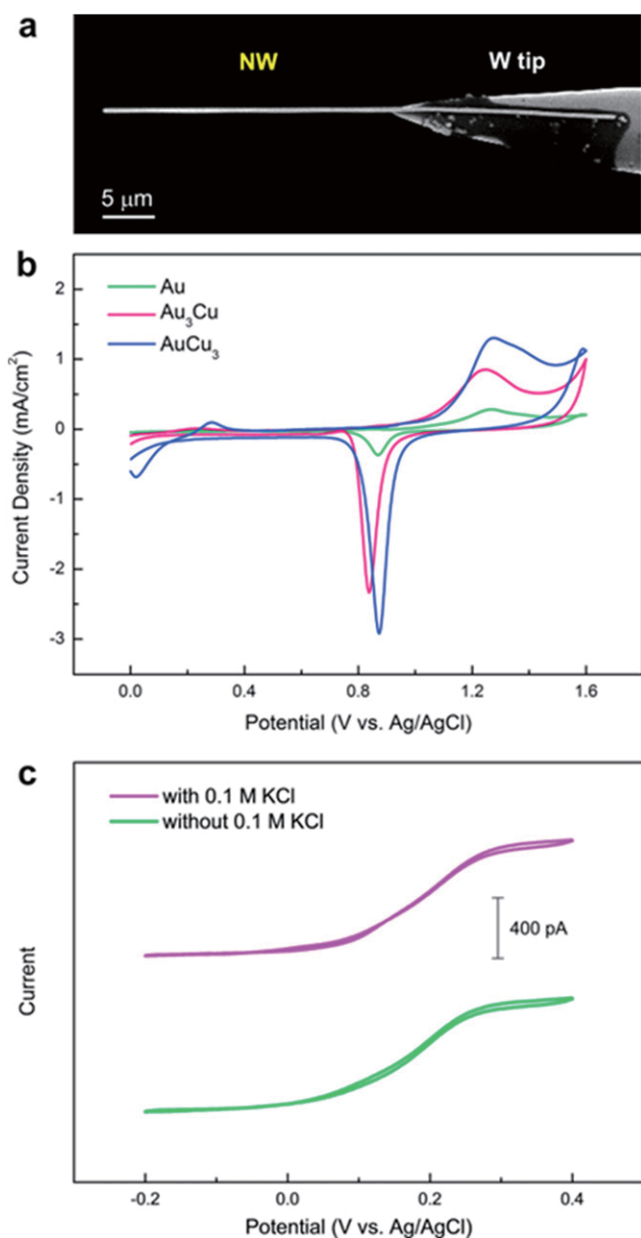


Figure 5. Electrochemical properties of NW electrodes. (a) SEM image of a NW electrode attached on W tip. (b) CVs of Au (green curve), Au₃Cu (pink curve) and AuCu₃ (blue curve) NW electrodes in a 50 mM H₂SO₄ at a scan rate of 50 mV s⁻¹. (c) CVs of Au₃Cu NW electrode in 20 mM K₃Fe(CN)₆ with or without 0.1 M KCl as supporting electrolyte at a scan rate of 2 mV s⁻¹.

only at the Au₃Cu NW electrode, it can be used for selective detection of glucose. In the mixture of glucose and AA, the current wave at -0.16 V is not affected by AA (blue curve). This selective oxidation current peak allows interference-free detection of glucose. The newly generated current wave is attributed to the synergistic effect of Au and Cu atoms in intermetallic Au₃Cu NW that has a different surface structure from Au NW [46, 47].

Figure 7 compares the calibration plots for glucose detection of Au and Au₃Cu NW electrodes. The current density data for CVs were obtained at -0.16 V. The CVs of Au NW electrodes show little current wave at this potential

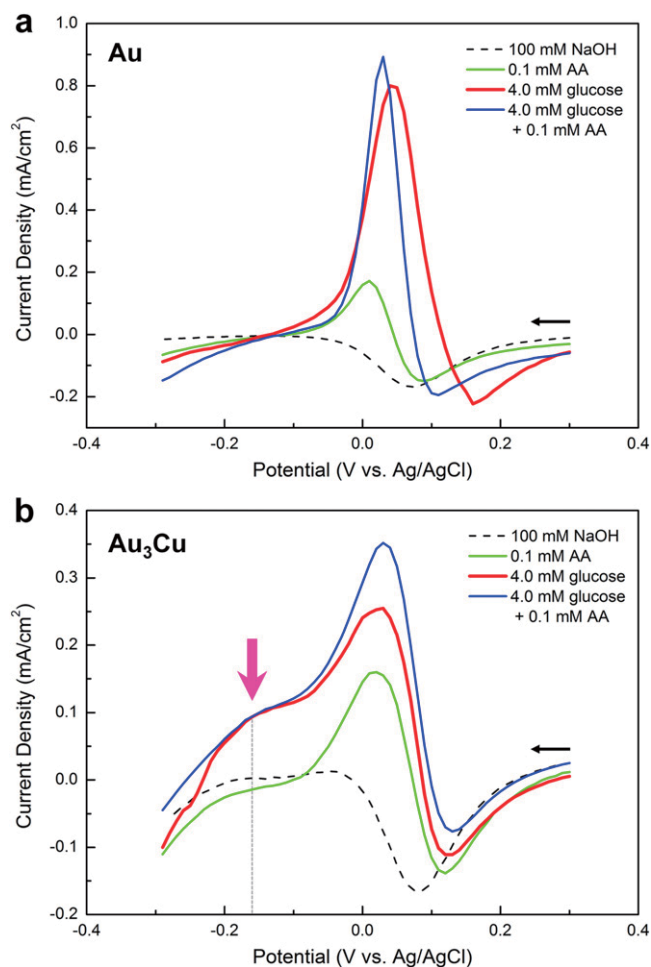


Figure 6. Reverse cathodic scans of CVs at (a) Au and (b) Au₃Cu NW electrodes in a 100 mM NaOH solution containing 4.0 mM glucose, 0.1 mM AA, and both glucose and AA. The scan rate is 100 mV s⁻¹.

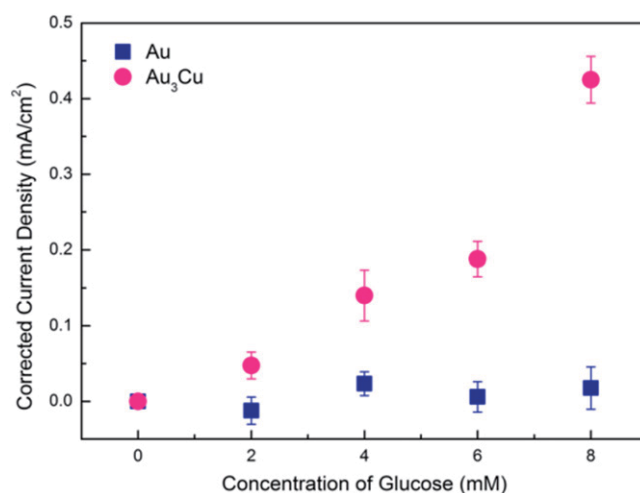


Figure 7. Background-subtracted calibration plots for glucose detection using Au (blue squares) and Au₃Cu NW (pink circles) electrodes in a 100 mM NaOH solution containing 0, 2.0, 4.0, 6.0, and 8.0 mM glucose. The data represent the mean plus the standard deviation from three measurements.

(blue squares). In contrast, the current densities of Au₃Cu NW electrodes increase with increasing concentration of glucose (pink circles), suggesting that quantitative and interference-free detection of glucose is feasible. In addition to interference-free detection of glucose, extremely small size of Au₃Cu NW electrodes can make them superb glucose probes for tiny biological systems such as cells. By employing these Au₃Cu NW electrodes, cellular glucose concentration can be directly monitored in real time.

4. Conclusions

Ordered intermetallic Au–Cu NWs were successfully synthesized via topotaxial transformation in gas phase. Pre-synthesized Au NWs were transformed into Au₃Cu and AuCu₃ NWs by supplying Cu-containing species. The compositions of Au–Cu NWs could be selected by adjusting the position of Au NW-grown substrates that react with Cu atoms. The single-crystalline nature of Au NWs was preserved after the transformation into Au₃Cu and AuCu₃ NWs. This simple topotaxial transformation method is a novel way to synthesize ordered intermetallic nanostructures without using surfactants. Because the electrochemical catalytic behavior of nanostructures can vary significantly with the atomic arrangement and surface conditions, ordered intermetallic NWs with an ultraclean surface may provide novel electrocatalytic properties [36, 48]. The present Au₃Cu NW electrodes show an additional current wave for glucose oxidation at –0.16 V, enabling selective glucose detection without the interference by AA. We propose that the ordered intermetallic Au–Cu NWs could be quite valuable for monitoring glucose levels in a single cell and can be further employed in diverse electrocatalysis in a microsystem.

Supporting information

TEM analysis of ordered intermetallic Au₃Cu and AuCu₃ nanoplates (figures S1 and S2). SEM images of the annealed Au NWs in the absence of CuI precursor (figure S3). TEM analysis for the oxidation resistant property of the AuCu₃ NWs (figure S4). Schematic of fabrication process for individual NW electrode (figure S5).

Acknowledgments

This work was supported by the Public welfare & Safety research program (NRF-2012M3A2A1051686) through the National Research Foundation of Korea funded by the Ministry of Science, ICT & Future Planning (MSIP), Global Frontier Project (H-GUARD_2014M3A6B2060489) through the Center for BioNano Health-Guard funded by the MSIP, and KRIBB initiative Research Program. TEM analysis was performed at the KBSI in Daejeon.

References

- [1] Fang X, Zhai T, Gautam U K, Li L, Wu L, Bando Y and Golberg D 2011 ZnS nanostructures: from synthesis to applications *Prog. Mater. Sci.* **56** 175–287
- [2] Liu H, Zhang Z, Hu L, Gao N, Sang L, Liao M, Ma R, Xu F and Fang X 2014 New UV-A photodetector based on individual potassium niobate nanowires with high performance *Adv. Opt. Mater.* **2** 771–8
- [3] Hamann S, Brunken H, Salomon S, Meyer R, Savan A and Ludwig A 2013 Synthesis of Au microwires by selective oxidation of Au–W thin-film composition spreads *Sci. Technol. Adv. Mater.* **14** 015003
- [4] Fang X, Hu L, Huo K, Gao B, Zhao L, Liao M, Chu P K, Bando Y and Golberg D 2011 New ultraviolet photodetector based on individual Nb₂O₅ nanobelts *Adv. Funct. Mater.* **21** 3907–15
- [5] Sinha S K, Srivastava C, Sampath S and Chattopadhyay K 2015 Tunability of monodispersed intermetallic AuCu nanoparticles through understanding of reaction pathways *RSC Adv.* **5** 4389–95
- [6] Hong X, Wang D, Yu R, Yan H, Sun Y, He L, Niu Z, Peng Q and Li Y 2011 Ultrathin Au–Ag bimetallic nanowires with coulomb blockade effects *Chem. Commun.* **47** 5160–2
- [7] Koenigsmann C, Santulli A C, Gong K, Vukmirovic M B, Zhou W-P, Sutter E, Wong S S and Adzic R R 2011 Enhanced electrocatalytic performance of processed, ultrathin, supported Pd–Pt core–shell nanowire catalysts for the oxygen reduction reaction *J. Am. Chem. Soc.* **133** 9783–95
- [8] Zhang H, Jin M, Wang J, Li W, Camargo P H C, Kim M J, Yang D, Xie Z and Xia Y 2011 Synthesis of Pd–Pt bimetallic nanocrystals with a concave structure through a bromide-induced galvanic replacement reaction *J. Am. Chem. Soc.* **133** 6078–89
- [9] Singh N, Dogan E, Karaman I and Arróyave R 2011 Effect of configurational order on the magnetic characteristics of Co–Ni–Ga ferromagnetic shape memory alloys *Phys. Rev. B* **84** 184201
- [10] Liu Z, Jackson G S and Eichhorn B W 2010 PtSn intermetallic, core–shell, and alloy nanoparticles as CO-tolerant electrocatalysts for H₂ oxidation *Angew. Chem. Int. Ed.* **49** 3173–6
- [11] Wang D, Xin H L, Hovden R, Wang H, Yu Y, Muller D A, DiSalvo F J and Abruña H D 2013 Structurally ordered intermetallic platinum–cobalt core–shell nanoparticles with enhanced activity and stability as oxygen reduction electrocatalysts *Nat. Mater.* **12** 81–7
- [12] Kang Y, Pyo J B, Ye X, Gordon T R and Murray C B 2012 Synthesis, shape control, and methanol electro-oxidation properties of Pt–Zn alloy and Pt₃Zn intermetallic nanocrystals *ACS Nano* **6** 5642–7
- [13] Deevi S C and Sikka V K 1996 Nickel and iron aluminides: an overview on properties, processing, and applications *Intermetallics* **4** 357–75
- [14] Vedantam T S, Liu J P, Zeng H and Sun S 2003 Thermal stability of self-assembled FePt nanoparticles *J. Appl. Phys.* **93** 7184–6
- [15] Abe H, Matsumoto F, Alden L R, Warren S C, Abruña H D and DiSalvo F J 2008 Electrocatalytic performance of fuel oxidation by Pt₃Ti nanoparticles *J. Am. Chem. Soc.* **130** 5452–8
- [16] Xia B Y, Wu H B, Wang X and Lou X W 2012 One-pot synthesis of cubic PtCu₃ nanocages with enhanced electrocatalytic activity for the methanol oxidation reaction *J. Am. Chem. Soc.* **134** 13934–7

- [17] Liu X, Wang A, Li L, Zhang T, Mou C-Y and Lee J-F 2011 Structural changes of Au-Cu bimetallic catalysts in CO oxidation: *in situ* XRD, EPR, XANES, and FT-IR characterizations *J. Catal.* **278** 288–96
- [18] Zhao W, Yang L, Yin Y and Jin M 2014 Thermodynamic controlled synthesis of intermetallic Au₃Cu alloy nanocrystals from Cu microparticles *J. Mater. Chem. A* **2** 902–6
- [19] Zhang N, Chen X, Lu Y, An L, Li X, Xia D, Zhang Z and Li J 2014 Nano-intermetallic AuCu₃ catalyst for oxygen reduction reaction: performance and mechanism *Small* **10** 2662–9
- [20] Ferrando R, Jellinek J and Johnston R L 2008 Nanoalloys: from theory to applications of alloy clusters and nanoparticles *Chem. Rev.* **108** 845–910
- [21] Schaak R E, Sra A K, Leonard B M, Cable R E, Bauer J C, Han Y-F, Means J, Teizer W, Vasquez Y and Funck E S 2005 Metallurgy in a beaker: nanoparticle toolkit for the rapid low-temperature solution synthesis of functional multimetallic solid-state materials *J. Am. Chem. Soc.* **127** 3506–15
- [22] Wang X-L, Feyngenson M, Chen H, Lin C-H, Ku W, Bai J, Aronson M C, Tyson T A and Han W-Q 2011 Nanospheres of a new intermetallic FeSn₅ phase: synthesis, magnetic properties and anode performance in Li-ion batteries *J. Am. Chem. Soc.* **133** 11213–9
- [23] Jana S, Chang J W and Rioux R M 2013 Synthesis and modeling of hollow intermetallic Ni-Zn nanoparticles formed by the Kirkendall effect *Nano Lett.* **13** 3618–25
- [24] Sra A K and Schaak R E 2004 Synthesis of atomically ordered AuCu and AuCu₃ nanocrystals from bimetallic nanoparticle precursors *J. Am. Chem. Soc.* **126** 6667–72
- [25] Wang G, Xiao L, Huang B, Ren Z, Tang X, Zhuang L and Lu J 2012 AuCu intermetallic nanoparticles: surfactant-free synthesis and novel electrochemistry *J. Mater. Chem.* **22** 15769–74
- [26] Yoo S M, Kang M, Kang T, Kim D M, Lee S Y and Kim B 2013 Electrotriggered, spatioselective, quantitative gene delivery into a single cell nucleus by Au nanowire nanoinjector *Nano Lett.* **13** 2431–5
- [27] Bai H, Han M, Du Y, Bao J and Dai Z 2010 Facile synthesis of porous tubular palladium nanostructures and their application in a nonenzymatic glucose sensor *Chem. Commun.* **46** 1739–41
- [28] Liu J and Xue D 2011 Rapid and scalable route to CuS biosensors: a microwave-assisted Cu-complex transformation into CuS nanotubes for ultrasensitive nonenzymatic glucose sensor *J. Mater. Chem.* **21** 223–8
- [29] Pang H, Lu Q, Wang J, Li Y and Gao F 2010 Glucose-assisted synthesis of copper micropuzzles and their application as nonenzymatic glucose sensors *Chem. Commun.* **46** 2010–2
- [30] Song Y-Y, Gao Z, Lee K and Schmuki P 2011 A self-cleaning nonenzymatic glucose detection system based on titania nanotube arrays modified with platinum nanoparticles *Electrochem. Commun.* **13** 1217–20
- [31] Lu W, Qin X, Asiri A M, Al-Youbi A O and Sun X 2013 Ni foam: a novel three-dimensional porous sensing platform for sensitive and selective nonenzymatic glucose detection *Analyst* **138** 417–20
- [32] Jiang L-C and Zhang W-D 2010 A highly sensitive nonenzymatic glucose sensor based on CuO nanoparticles-modified carbon nanotube electrode *Biosens. Bioelectron.* **25** 1402–7
- [33] Toghiani K E and Compton R G 2010 Electrochemical non-enzymatic glucose sensors: a perspective and an evaluation *Int. J. Electrochem. Sci.* **5** 1246–301
- [34] Yoo Y, Seo K, Han S, Varadwaj K S K, Kim H Y, Ryu J H, Lee H M, Ahn J P, Ihee H and Kim B 2010 Steering epitaxial alignment of Au, Pd, and AuPd nanowire arrays by atom flux change *Nano Lett.* **10** 432–8
- [35] Guglietta G, Wanga T, Pati R, Ehrman S and Adomaitis R A 2009 Chemical vapor deposition of copper oxide films for photoelectrochemical hydrogen production *Proc. SPIE* **7408** 740807
- [36] Miura A, Wang H, Leonard B M, Abruña H D and DiSalvo F J 2009 Synthesis of intermetallic PtZn nanoparticles by reaction of Pt nanoparticles with Zn vapor and their application as fuel cell catalysts *Chem. Mater.* **21** 2661–7
- [37] Seo K, Lee S, Yoon H, In J, Varadwaj K S K, Jo Y, Jung M-H, Kim J and Kim B 2009 Composition-tuned Co_nSi nanowires: location-selective simultaneous growth along temperature gradient *ACS Nano* **3** 1145–50
- [38] Lee H, Yoo Y, Kang T, In J, Seo M-K and Kim B 2012 Topotaxial fabrication of vertical Au_xAg_{1-x} nanowire arrays: plasmon-active in the blue region and corrosion resistant *Small* **8** 1527–33
- [39] Chyr I and Steckl A J 2001 GaN focused ion beam micromachining with gas-assisted etching *J. Vac. Sci. Technol. B* **19** 2547–50
- [40] Chen W, Yu R, Li L, Wang A, Peng Q and Li Y 2010 A seed-based diffusion route to monodisperse intermetallic CuAu nanocrystals *Angew. Chem.* **122** 2979–83
- [41] Xu Z, Lai E, Shao-Horn Y and Hamad-Schifferli K 2012 Compositional dependence of the stability of AuCu alloy nanoparticles *Chem. Commun.* **48** 5626–8
- [42] Cheng T-M, Huang T-K, Lin H-K, Tung S-P, Chen Y-L, Lee C-Y and Chiu H-T 2010 (110)-Exposed gold nanocoral electrode as low onset potential selective glucose sensor *ACS Appl. Mater. Interfaces* **2** 2773–80
- [43] Park S, Chung T D and Kim H C 2003 Nonenzymatic glucose detection using mesoporous platinum *Anal. Chem.* **75** 3046–9
- [44] Solla-Gullón J, Vidal-Iglesias F J, López-Cudero A, Garnier E, Feliu J M and Aldaz A 2008 Shape-dependent electrocatalysis: methanol and formic acid electrooxidation on preferentially oriented Pt nanoparticles *Phys. Chem. Chem. Phys.* **10** 3689–98
- [45] Lee H, Habas S E, Somorjai G A and Yang P 2008 Localized Pd overgrowth on cubic Pt nanocrystals for enhanced electrocatalytic oxidation of formic acid *J. Am. Chem. Soc.* **130** 5406–7
- [46] Chen L Y, Fujita T, Ding Y and Chen M W 2010 A three-dimensional gold-decorated nanoporous copper core-shell composite for electrocatalysis and nonenzymatic biosensing *Adv. Funct. Mater.* **20** 2279–85
- [47] Shi H, Zhang Z, Wang Y, Zhu Q and Song W 2011 Bimetallic nano-structured glucose sensing electrode composed of copper atoms deposited on gold nanoparticles *Microchim. Acta* **173** 85–94
- [48] Li D, Wang C, Tripkovic D, Sun S, Markovic N M and Stamenkovic V R 2012 Surfactant removal for colloidal nanoparticles from solution synthesis: the effect on catalytic performance *ACS Catal.* **2** 1358–62